International Journal of Heat and Mass Transfer 182 (2022) 121865

Contents lists available at ScienceDirect

International Journal of Heat and Mass Transfer

journal homepage: www.elsevier.com/locate/hmt

Heat transfer and pressure drop correlations for direct on-chip microscale jet impingement cooling with alternating feeding and draining jets

Tiwei Wei[a,b,*], Herman Oprins[a], Liang Fang[b], Vladimir Cherman[a], Eric Beyne[a], M. Baelmans[b]

[a] IMEC, Leuven 3001, Belgium
[b] Departement of Mechanical Engineering, KU Leuven, Leuven 3001,Belgium

ARTICLE INFO

Article history:
Received 10 March 2021
Revised 5 July 2021
Accepted 15 August 2021
Available online 1 October 2021

Keywords:
Impingement jet cooling
Scaling analysis
Unit cell
Nusselt correlations
Friction factor

ABSTRACT

Jet impingement cooling with distributed outlet configuration is regarded as an efficient cooling solution for high performance systems. This work develops the Nusselt number $\overline{Nu}_f$-Re_d and pressure drop k-factor correlations for microscale multi-jet impingement cooling with alternating feeding and draining jets. An extensive design of experiments (DOE) of unit cell modeling-based simulations is used for the correlation fitting. In order to understand the flow and thermal behavior, the impact of single variables including the inlet diameter, outlet diameter, jet-to-target distance and nozzle length is studied systematically. On the other hand, this work firstly shows the predictive model with k-Re_d, including the impact of nozzle length t/L, cavity height H/L and inlet diameter ratio d_i/L. Finally, the extracted correlations are experimentally validated, both with experimental data of different jet impingement demonstrators, as well as with the literature experimental data.

1. Introduction

Jet impingement cooling on the chip backside is very promising due to the high heat transfer rates and the absence of thermal interface material. The most commonly considered impingement jet cooling implementation in literature is based on the common outlet configuration, shown in Fig. 1. In this configuration, the jet flow is injected through nozzle arrays and extracted through the outlets on the edges of the cooler. However, the disadvantage of jet impingement cooling with a common return is that the heat transfer can be highly influenced by the "cross-flow effects" where the return flows interact with the jets flow [1–3]. The cooling performance of jet cooling can be significantly affected by a large number of jets, especially for large die area applications. Kercher and Tabakoff [4] and Florschuetz et al. [5] experimentally examined the detrimental effect of the crossflow on the heat transfer coefficient. Maddox et al. [2] investigated methods to manage the spent flow, such as angled confining walls and anti-crossflows (ACF) cooling structures or corrugated jet planes. Hollworth and Dagan [6] found that the convective coefficients can be improved with 20–30% by arranging the outlet nozzles through the impingement surface. However, this is not applicable for cooling on the electronic devices. The second configuration, jet Impingement cooling with alternating feeding and draining jets shown in Fig. 1(b) is a more appealing variant for electronic cooling [7,8], where the spent fluid can be efficiently extracted through the outlet nozzles that are distributed in between the inlet nozzles [1–3,7]. In the next sections, a literature overview is provided for both nozzle configurations.

1.1. Configuration A: common outlets

Empirical correlations for heat transfer and pressure coefficient are very important to understand the functional relations regarding different geometry parameters. Extensive literature studies about single impingement jet cooling correlations covering different nozzle geometries for both submerged and free-surface jet configurations are published in the last decades [9–12]. Garimella and Rice [13] developed $\overline{Nu}_d$ correlation for a single confined circular submerged jet. Womac et al. [14] developed correlations for a single circular free-surface jet. The correlations with a single round nozzle, orifice, or pipe are developed by Martin [15].

Compared to single jet impingement, arrays of multiple jets can achieve a higher heat transfer rate and more uniform temperature distribution [16]. Weigand and Spring [17] summarized and com-

* Corresponding author at: IMEC, Leuven 3001, Belgium.
E-mail address: tiwei32@stanford.edu (T. Wei).

https://doi.org/10.1016/j.ijheatmasstransfer.2021.121865
0017-9310/

Nomenclature

A	chip area mm^2
Bi	Biot number
d_i	inlet diameter μm
d_o	outlet diameter μm
f	friction loss coefficient
H	standoff between the jet exit and the chip μm
K	pressure coefficient
k_{si}	thermal conductivity of silicon W/mK
k_{fl}	thermal conductivity of the fluid W/mK
L	unit cell length μm
$\overline{Nu_f}$	Nusselt number based on average interface temperature of the chip
$\overline{Nu_j}$	Nusselt number based on average junction temperature
Pr	Prandtl number
R_{th}	thermal resistance K/W
$R_{th}{}^*$	normalized thermal resistance $K.cm^2/W$
Re_d	Reynolds number
S_d	chip size (length = width) μm
$\bar{T}_{chip}$	average temperature of the heat source °C
T_{in}	coolant inlet temperature ° C
T_{amb}	ambient temperature ° C
$\overline{T_s}$	average cooling surface temperature ° C
t	nozzle thickness μm
t_c	chip thickness μm
$\bar{V}_{in}$	inlet velocity m/s
ΔP	pressure difference between the inlet and outlet of the cooler Pa
ΔT_{avg}	chip temperature increases ° C
α	dimensionless inlet nozzle diameter d_i/L
β	dimensionless outlet nozzle diameter d_o/L
γ	dimensionless nozzle length t/L
φ	dimensionless cavity height H/L

Subscripts

avg	average
ch	channel
i/in	inlet
o/out	outlet
hs	hotpots of the heater
n	nozzle
p	pumping
tot	total
th	thermal

pared the existing empirical correlations of multiple impinging air jets for average and locally resolved heat transfer coefficients, respectively. Narumanchi et al. [18] reported that there is a good match between CFD results and experimental data from Womac et al. [14] over a wide range of Reynolds numbers for confined and unconfined submerged jets. Whelan and Robinson [19] reported that the confined submerged nozzles with contoured inlet or inlet/outlet are the suggested nozzle configurations. Florschuetz et al. [5] developed the correlations for the inline and staggered nozzle patterns, and concluded that the staggered patterns resulted in smaller heat transfer coefficients than their inline counterparts. Besides, Royne and Dey [20] also investigated the effect of nozzle geometry on the heat transfer and pressure drop to confined-submerged jet arrays over a Reynolds number range of $1000 \leq Re_D \leq 7700$. It is reported that the sharp-edged and contoured nozzles can enhance the cooling performance in comparison to the conventional straight nozzle arrays for a given pumping power.

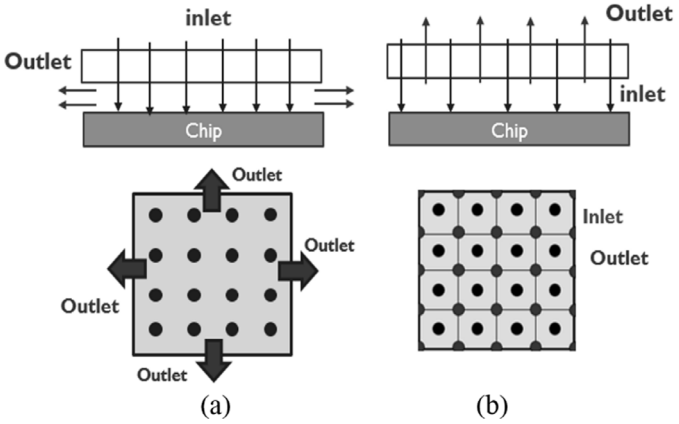

Fig. 1. Impingement jet cooling configurations: (a) configuration A: common outlets and (b) configuration B distributed outlets configurations.

Azar [21] and Molana and Banooni [22] both present various average heat transfer coefficient for single-phase liquid correlations. Martin [23] developed correlations for multiple circular submerged jets. Patil and Narayanan [24] proposed a criterion value S_{NN}/d for negligible cross flow, and made a correction of Martin's correlation. The Womac et al. [25] correlation divided the entire heat transfer area into two separate regions: the "impingement zone" and the "wall-jet region" outside of the impingement zone. Experiments conducted for the confined-submerged liquid jet arrays found that the heat transfer coefficient was somewhat insensitive to jet to-target spacing within the range of $2 \leq H/D \leq 4$ due to the target surface being within the potential core of the issuing jets. Robinson and Schnitzler [26] conducted experiments investigating the impingement of water jet arrays under both free-surface and submerged conditions. For the submerged jets, it was found that heat transfer was insensitive to jet-to-target spacing changes in the range of $2 \leq H/D \leq 3$. A monotonic decrease in heat transfer was observed with increasing jet-to-target spacing in the range of $5 \leq H/D \leq 20$. It was also found that a stronger dependence on jet-to-jet spacing was encountered for smaller jet-to-target spacing. The effect of jet-to-jet spacing for jet arrays was more closely examined by Pan and Webb [27]. For the central jet module, the stagnation point heat transfer coefficient was found to be independent of jet-to-jet spacing. Conversely, a dependence on the jet-to-target spacing was discovered. The more recent work of Fabbri and Dhir [28] involved both heat transfer to the jet arrays and the associated pressure drop across the jet nozzle plate.

The Reynolds correlations for stagnation Nusselt number and average Nusselt number are summarized in Table 1, together with the methodology and the range for the Re_d and H/D. In general, there is an abundance of $\overline{Nu_f}$-Re_d correlations for impinging jets cooling in the literature, and they generally show $Nu \sim a \cdot Re_d{}^b$, where the exponent b is typically in the range of 0.5–0.8. However, most of the correlations derived from the analytical predictions were based on the simplified assumption that each impinging jet formed an individual cell or module. The local and average heat transfer rates were determined for repeating modules surrounding each jet in the array. These correlations are valid when the jet-to-target distance and jet-to-jet spacing were larger, and the jet-to-jet interactions are negligible. Since the jets were well-drained, there was negligible crossflow between neighboring jets, and each jet established a cell that behaved thermally as a single isolated impinging jet.

Table 1
State of the art Nusselt-Reynolds correlation for common outlets.

Source	Description	Provides	Methodology	**Conditions**	**Reynolds exponent**	**Reynolds number, cavity height range**
Martin [23]	Submerged, multiple, circular	$\overline{Nu}_d$	Analytical	Tref=Tin	0.67	2000<Re<100,000; 2≤H/D≤12
Martin [23]	Single, circular, submerged	$\overline{Nu}_d$	Analytical	Tref=Tin	0.775	2000<Re<40,000; 2≤H/D≤12
Womac (1994)	Multiple jets, submerged, circular	$\overline{Nu}_{d+L}$	Analytical	Tref=Tin	0.5/0.8	5000<Re<200,000; 2≤ S/D≤4
Womac (1994)	Single, submerged, circular	$\overline{Nu}_{d+L}$	Analytical	Tref=Tin	0.5/0.8	Re< 5000; 2≤ S/D≤4
Elison and Webb [39]	Submerged, single jet, circular	Nu_0	Experiment	Tref=Tin	0.8	300 < Re < 7000; H/D<8
Garimella and Rice [13]	single, confined/submerged, circular	Nu_0	Experiment	Tref=Tin	0.585	4000<Re<23000; 1≤ S/D≤5
Lee and Vafai (1999)	Submerged, Multiple, circular	$\overline{Nu}_d$	Analytical	Tref=Tin	0.667	2000<Re<100000; 2≤H/D≤12
Li and Garimella [40]	Single jet, circular, confined/submerged	$\overline{Nu}_{1.9d+d}/Nu_0$	Experiment	Tref=Tin	0.5555/ 0.515	4000 <Re< 23000; 1≤H/D≤5
Robinson and Schnitzlaer [41]	Submerged, jet array, circular	$Q_{pump}/\overline{Nu}_{d/2}$	Experiment	Tref=Tin	0.46	100 < Re < 10000; 2≤H/D≤ 20; 3 ≤ P/D ≤ 7
Meola [42]	Air/water, confined, circular, jet arrays	$\overline{Nu}_d$	Analytical	Tref=Tin	0.68	200<Re<100,000; 1.6<H/D<20
Tie et al. [43]	Submerged, jet arrays	$\overline{Nu}_d$	Experiment	Tref=(Tin+Tout)/2	0.51	1398.113≤Re ≤13440.4; 4.963≤Pr≤ 9.311
Yonehara and Ito [44]	Free surface, liquid, multiple jets	$\overline{Nu}_d$	Analytical	uniform temp	0.67	Re<48000 P/D>13.8
Jiji and Dagan [45]	Free surface, liquid, single phase, multiple jets	$\overline{Nu}_L$	Experiment	uniform heat flux	0.5	0.5 mm and 1.0 mm 3 mm < z < 10 mm L=heater length
Fabbri and Dhir [28]	Free surface, liquid, single phase, multiple jets	$\overline{Nu}_d/\Delta p$	Experimental	water and FC40	0.78	73 < Re < 3813 65μm < dn < 250μm
Vader et al. [46]	Liquid, planar, confined,	Nu_0	Numerical	water	0.5	20000<Re<90000, 2.7<Pr<4.5
Liu et al. [47]	Liquid jet, free surface, single phase	Nu_0	Analytical and experimental	water	0.5	0≤r/d<0.787 0.15≤Pr≤3
Michna et al. [48]	Submerged/confined/ microjet arrays/ single phase	$\overline{Nu}_d$	Experiment	Tref=Tin	0.55	50 < Red < 3500; D=54 and 112 μm
Muszynski and Andrzejczyk [49]	Confined, multiple	$\overline{Nu}_d$	Experiment	LMTD	0.65	500<Re<2500

1.2. Configuration B: distributed outlets

The description of correlations for configurations with local extraction of the spent fluid to a plenum is very limited in literature. The concept of a jet impingement array cooling with local effusion nozzles was first proposed by Huber and Viskanta [29]. They developed $\overline{Nu}_f$ correlations based on the experimental data for a confined 3 × 3 array with a center jet and spent air exit ports. The validated ranges of the parameters for the correlation are: $3400 < Re_D < 20500$, $4 < X_n/D < 8$ and $0.25 < H/D < 6.0$. The obtained experimental data can be applied to Martin's correlation [23] since both of them are based on the spent air exits and without considering the crossflow effect. Rhee et al. [30] employed a naphthalene sublimation method to determine local heat/mass transfer coefficients on the target plate. They found that the heat/mass transfer for the smaller nozzle to target distance is improved significantly and the augmented values are 60% and 20% higher for H/D = 0.5 and 1.0, respectively than those without the effusion holes. However, the performance with the cooling performance with the effusion holes is similar to those without the effusion holes for large gap distances.

Onstad et al. [3,31] showed that a geometry which incorporates local extraction with a large exhaust area ratio, A_e/A_{jet}, is preferred to maintain a high average heat transfer coefficient. Three different impingement arrays were studied, all of which had a jet-to-jet spacing of $Z_n/D = 2.34$, jet-to-target spacing of H/D = 1.18, and extraction holes in the jet plane. Brunschwiler [7] demonstrated and experimentally characterized the microscale liquid jet impingement array cooling will locally distributed outlets, where the number of inlet nozzles is up to 47,000. A simple heat transfer correlation was developed based on the experimental data with a ± 9% confidence level. The experimental data were measured at H/D = 1.2, which is in the stable impingement regime. Furthermore, the Reynolds number Re is below 800, which means the considered flow is laminar. Hoberg et al. [32] evaluated a new nozzle array configuration with six small extraction ports centered around each injection nozzle. A Nu-Re correlation was proposed for laminar-to-turbulent flow, where the Reynolds number is in the range of 500–10,000. However, this correlation was only extracted at H/D = 1. Rattner [33] developed new correlations for Nusselt number and pressure-drop k-factors based on 1000 randomized cases. The pressure-drop k -factor is calculated based on the inlet and outlet boundary pressure difference, correcting for frictional losses in the injection and return channels. The new correlations for pressure drop (k -factor) and heat transfer performance (Nusselt number, $\overline{Nu}_f$) are valid over a wide range of Reynolds number (Re_j = 20–500), fluid transport properties (Pr = 1–100), and component geometries (p/D_j = 1.8–7.1 and th/D_j = 0.1–4.0).

The objective of this study is to predict the thermal and hydraulic performance of multiple jet impingement cooling with locally distributed outlets. For that the dimensionless correlations will be derived and validated in this paper. Firstly, the modeling studies based on unit cell model will be introduced in Section 2. After that, the design of experiment (DOE) and fitting of the correlations based on the dimensionless parameters are investigated systematically in Section 3. The individual parameters impact is shown in Section 3.2 and the combined parameters effects are presented in Section 3.3. The correlations for the Nusselt number and pressure coefficient factor, as a function of the Reynolds number and all relevant geometrical parameters are developed.

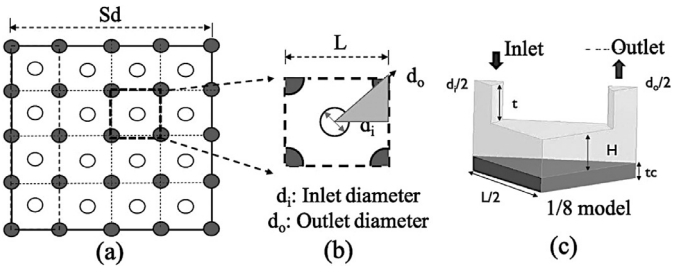

Fig. 2. CFD model of the unit cell model extracted from the full cooler model: (a) top view of the nozzle arrays; (b) unit cell model with single inlet and four outlets; (c) 1/8 unit cell model.

Section 4 shows the experimental validations of the fitted correlations with the inhouse experimental results and also the literature measurement data.

2. Numerical approach

2.1. Geometric configuration of unit cell model

The schematic of the jet impingement cooling with distributed outlets model is shown in Fig. 2, for an 8 × 8 mm^2 chip. The liquid coolant for this study is DI water. The impingement cooler geometry contains N × N array of inlet nozzles and distributed outlets in between the inlets. After striking on the chip surface, the fluid returns to the outlet plenum through the effusion nozzles. The inlet nozzles and outlet nozzles are both distributed on the nozzle plate, where one inlet is surrounded by four outlets. The top view of the nozzle plate with nozzle arrays presents quasiperiodic behavior. As shown in Fig. 2, the impingement jet cooler with an N × N jet array, there are five design parameters needed to be considered for the cooler geometry design: d_i, d_o, H, t, t_c, L, where d_i is the inlet diameter, d_o is the outlet diameter, t_c represents the chip thickness, H is the standoff between the jet exit and the heater, t is the nozzle thickness, and L is the unit cell length, which is defined as below:

$$L = \frac{A}{N \times N} \tag{1}$$

where A is the chip area. L also represents the pitch between the two neighboring inlet jets. Also, the flow and thermal parameters as the input conditions are listed as: $\bar{V}_{in}$ and T_{in}, where T_{in} is the inlet temperature, and $\bar{V}_{in}$ is the inlet velocity.

In order to simplify the N × N nozzle arrays, unit cell with only one inlet surrounded by four ¼ outlet with symmetry boundary conditions can be used. For the further reduction of the computation cost, 1/8 model simplified from the unit cell model is introduced, which can highly reduce the computation cost [36]. The nozzle number N is actually determined by the inlet nozzle pitch L, as shown in Fig. 2b for a constant chip size S_d assumption. Therefore, as we scale the nozzle pitch L, then the nozzle number N will also change correspondingly as $N = S_d/L$. The impact of the nozzle number is therefore modeled by changing the size of the unit cell model, while maintaining a constant heat flux boundary condition.

2.2. Unit cell model method

The conjugate heat transfer models consider conduction and convection in the liquid domain of the model and conduction in the solid domain. In this paper, conjugate heat transfer and fluid dynamics simulations (CHT CFD) have been performed to assess the thermal and fluidic behavior of an impingement cooler with N × N nozzles array based on ANSYS FLUENT 18.0 [10]. This solid domain represents the silicon die only. The rest of the solid can be neglected due to the high cooling transfer rate of the jet cooling. Our previous study shows that the thermal conductivity of the cooler materials has negligible effects on the cooler thermal and hydraulic performance [8]. A transition shear stress transport (SST) model is used for the CFD simulations, since this type of turbulence model offers a good compromise between accuracy and computational time for jet impingement modeling and allows to cover the large range of Re numbers from laminar flow, over transitional flow to turbulent flow that is encountered in practical cooling design. Moreover, the benchmarked studies shows that SST model can predict the local or average Nu, and also local level pressure coefficient f with less than 5% difference in the range of 30 < Red < 4000, compared with the reference Large eddy simulation (LES) model [34]. The reported laminar to turbulence transition range for liquid jet impingement is between 1000 and 3000 [12]. Based on this range of considered Re numbers from laminar to low Re turbulent flow, a RANS based transition SST model has been chosen [34], using the "Semi Implicit Method for Pressure Linked Equations (SIMPLE)" [17] algorithm as the solution method and the Quadratic Upstream Interpolation for Convective Kinematics (QUICK) scheme [17,18] for the numerical discretization. The power dissipation in the chip is represented as a heat flux boundary condition on the Si. The flow conditions are applied as a velocity condition at the inlet and a pressure outlet boundary condition for the outlet. For the model material properties, the density, viscosity and other material properties of the fluid/solid are assumed to be constant during the simulation. All cavities are assumed to be completely filled with the liquid coolant, without any the presence of air (submerged jets).

For the meshing of the CFD models, hybrid meshing is chosen. The fluid domain mesh is chosen as tetrahedron mesh cells. Prism element cells are used for the meshing of the boundary layers with minimal meshing size of 0.002 mm. The latter is calculated from the y + < 1 constraint for the turbulence model near boundaries [5]. The number of boundary layer grid cells in the normal direction to solid walls is set to 15. For the solid domain mesh prism cells are used with a 20 μm mesh size. The grid convergence index (GCI) is used for the meshing sensitivity analysis. The GCI_{12} and asymptotic range of convergence are evaluated for the unit cell model. The grid sensitivity analysis using the Richardson extrapolation [5] predicts a discretization error for the stagnation temperature of 0.2%. The details of the mesh for the unit cell model can be found in our previous study [34].

For the boundary conditions of the unit cell modeling, a Dirichlet boundary condition is used which means the velocity of the liquid at all fluid–solid boundaries are equal to zero (no slip condition). The boundary condition for the cooler inlet is set as a constant uniform inlet velocity while the static pressure for the outlet is set to 0 Pa, as a reference pressure. This means all pressure data obtained are specified relatively to the outlet pressure. As for the thermal boundary conditions, the coolant inlet temperature is set as a constant temperature. Moreover, constant heat flux is applied on the chip bottom to represent the power generation in the heating elements of the test chip. In addition, the bottom package of the chip is regarded as thermal insulation. The fluid and solid interface is set as a flow-thermal coupled boundary condition. The convergence criteria for the unit cell modeling is set at 10–5 for continuity, 10–6 for energy and 10–6 for k, w and momentum (x, y and z velocities), respectively.

Fig. 3(b) shows an example of the unit cell modeling results of 4 × 4 inlet jet arrays with chip surface temperature distributions for different nozzle diameters. The temperature distribution in the Si and the pressure drop between inlet and outlet will be used in the next sections. Uniform velocity profile is applied on the inlet boundary, and pressure out boundary condition is applied on the outlet surface. The applied heat flux is 37.5 W/cm^2. The inlet

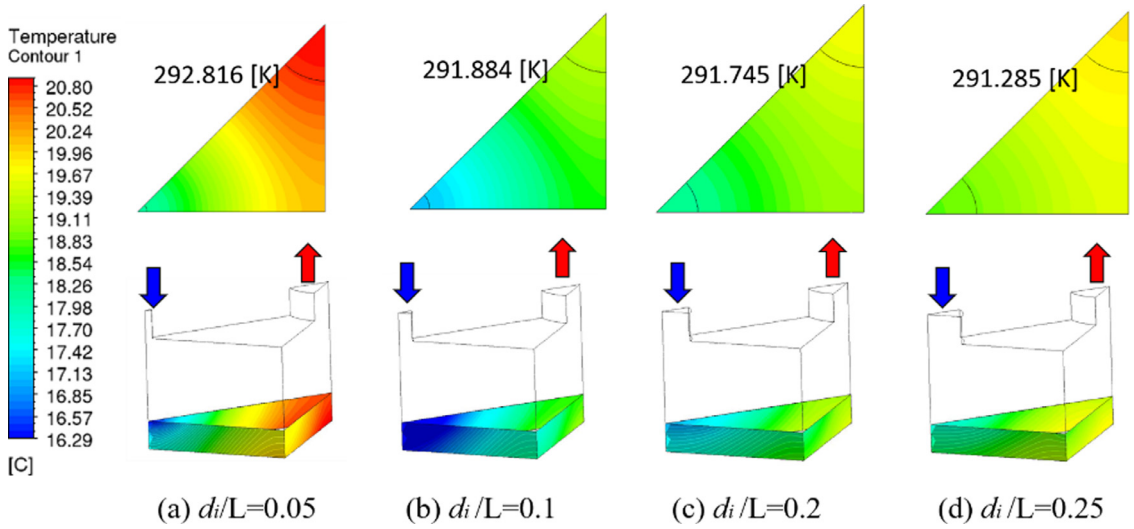

Fig. 3. Temperature distribution for different inlet diameter d_i/L: (a) d_i/L = 0.05; (b) d_i/L = 0.1; (c) d_i/L = 0.2; (d) d_i/L = 0.25. (d_O/L = 0.3, t/L = 0.1, and H/L = 0.3, Re_d = 1024)

temperature is kept as 10 °C. The temperature distributions across the chip surface and symmetric faces can be visualized. It can be seen that the temperature reduces as the inlet diameter becomes larger. For small d_i/L, the stagnation region and wall jet region are very limited, resulting in a higher temperature at the outlet region. Moreover, the heat spreading through the silicon die dominates as the inlet diameter is very small. As the inlet diameter becomes larger, the jet cooling stagnation region becomes larger and the temperature drops. The impact will be studied in details in the next sections.

3. Correlations development

3.1. Dimensionless analysis definition

The previous parametric analysis shows that there are a lot of parameters included in the cooler geometry [35]. When the nozzle number N is scaling, the other parameters are changed too. Therefore, it is necessary to normalize the parameters to simplify the design. The dimensionless analysis is known as a very powerful tool to understand the physics in the area of heat transfer and fluid mechanics. It specifies that the normalized physical behavior of the impingement cooler is determined by the normalized proportions of the geometrical design parameters (the dimensionless parameters), and also the normalized flow conditions. This phenomenon can be exploited to generalize the obtained modeling results and to understand the fundamental behavior of the multi-jet impingement cooler.

Taking advantage of the Buckingham π theorem, the abovementioned geometrical parameters and input/output parameters in Section 2.1 are transferred to the dimensionless form. As a dimensionless number of the heat transfer using d_i as the characteristic length scale, the Nusselt number in the unit cell is defined as below, with two definitions:

(1) Nusselt number based on average interface temperature of the chip:

$$\overline{Nu}_f = \frac{\overline{h}_f\, d_i}{k_{fl}} = \frac{\dot{Q}}{A\cdot\Delta T}\cdot\frac{d_i}{k_{fl}} = \frac{q\ \cdot d_i}{\left(\overline{T}_s - T_{in}\right)\cdot k_{fl}} \tag{2}$$

(2) Nusselt number based on average junction temperature:

$$\overline{Nu}_j = \frac{\dot{Q}}{A\cdot\Delta T}\cdot\frac{d_i}{k_{fl}} = \frac{q\ \cdot d_i}{\left(\overline{T}_{chip} - T_{in}\right)\cdot k_{fl}} \tag{3}$$

This term $\overline{Nu}_j$ is actually used to correlate with the experiments. This quantity includes the impact of the conduction in the Si.

The Reynolds number and the Prandtl number are defined as following:

$$Reynolds\ number: Re_d = \frac{\rho d_i \overline{V}_{in}}{\mu} \tag{4}$$

$$Prandtl\ number: Pr = \frac{\mu Cp}{k_{fl}} \tag{5}$$

where k_{fl} is the thermal conductivity of the fluid, μ is the dynamic viscosity, and Cp is the specific heat. In addition, the $\overline{T}_s$ shown in $\overline{Nu}_f$ is the fluid and solid interface temperature, while $\bar{T}_{chip}$ is based on the junction temperature. Since the focus of this study is the geometrical aspect, the fluid properties are kept constant in this study. Therefore, the Prandtl number used in this work is fixed as 7.56, a representative value for DI water.

In order to generalize the parametric trend, we need to extract the relation between the geometrical flow parameters and normalized heat transfer in the following form:

$$\overline{Nu}_f = f\left(Re_d,\ \frac{d_i}{L},\ \frac{d_o}{L},\ \frac{H}{L},\ \frac{t}{L}\right)$$

$$\overline{Nu}_J = f\left(Re_d,\ \frac{d_i}{L},\ \frac{d_o}{L},\ \frac{H}{L},\ \frac{t}{L},\ \frac{t_c}{L}\right) \tag{6}$$

where $\overline{Nu}_f$ is the area averaged Nusselt number as function of the jet diameter $\frac{di}{L}$ and the other dimensionless variables. And also, the $\frac{t_c}{L}$ is not included in $\overline{Nu}_f$ function. The chip thickness impact is actually included in $\overline{Nu}_J$. If the convective heat transfer increases, the contribution of the thickness becomes more significant.

The dimensionless number for the pressure-drop k-factor can be expressed as following:

$$k = f\left(Re_d, \frac{d_i}{L},\ \frac{d_o}{L},\ \frac{H}{L},\ \frac{\mathrm{t}}{L}\right) \tag{7}$$

$$k = \frac{\Delta P}{\left(\frac{1}{2}\rho\cdot\bar{V}_{in}^2\right)} \tag{8}$$

where k is the pressure coefficient, and t is the thickness of the nozzle plate. ΔP is defined as the pressure drop between the inlet and outlet nozzle at the unit cell level.

Table 2
List of dimensionless variables and range.

Parameter	Symbol	Range
Re_d	Re_d	32,64,128,216,512,1024,2048
d_i/L	α	0.01,0.1,0.2,0.3,0.4
d_o/L	β	0.05–0.5
t/L	γ	0.1–1.2
H/L	φ	0.05–2

As discussed in this section, the $\overline{Nu}_f$-Re_d curves are the same for different nozzles arrays with the same dimensionless parameter ratios. Therefore, a single nozzle number N investigation can be used for the extraction of the correlations for $\overline{Nu}_f$-Re_d and k-Re_d. The fitted predictive models can be used to extract the thermal and hydraulic performance for arbitrary nozzle numbers.

In the following section, an extensive design of experiments will be conducted by varying the dimensionless numbers. The dimensionless parameters include d_i/L, d_O/L, H/L, t/L, and t_c/L. The analysis is based on a fixed chip size A, with nozzle array of N × N. The study range for the dimensionless analysis parameter is listed in Table 2.

3.2. Variable impact analysis

In this section, the DOE analysis based on the listed dimensionless parameters in Table 2 is presented: Section 3.2 shows the individual effect of the geometrical parameters, and the scaling trend fitted as function, to decouple the effects of other parameters; Section 3.3 presents the combined effects using the derived functions from Section 3.2 as basis for the fitting of the large DOE.

3.2.1. Heat spreading effects in silicon chip

In our test case, the thermal test chip is flip-chip bonded on the substrate, while the active heater region is at the bottom of the chip. Therefore, the junction temperature T_j is higher than the interface temperature T_s due to the heat conduction through silicon, resulting in an additional thermal resistance. For high performance cooling, this add resistance can be significant, and even the dominant contributor. In general applications, junction temperature T_j can be measured. For the evaluation of the cooling performance, T_s is needed. This section will discuss what is the relation between $\overline{Nu}_j$ and $\overline{Nu}_f$, and also how does it impact with the N scaling.

As defined in Section 3.1, $\overline{Nu}_j$ is based on the junction temperature while $\overline{Nu}_f$ is based on the fluid-solid interface temperature. This means that the chip thickness effect is not included in the $\overline{Nu}_f$. Considering a simplified thermal resistance network, the total thermal resistance between junction and coolant contains three parts: heat convection of the jet cooling, 1D heat conduction through the Si and additional heat spreading effects through the silicon substrate. Thus, we can get the following equation:

$$R_{th} = \frac{1}{\bar{h}_f A} + \frac{t_c}{k_s A} + R_{spreading} \tag{9}$$

$$R_{th} = \frac{1}{\bar{h}_j A} \tag{10}$$

where R_{th} is the thermal resistance based on the average junction temperature. A is the chip area. The equivalent heat transfer coefficient based on the average cooling interface temperature is defined as $\bar{h}_f$ while $\bar{h}_j$ is defined as the heat transfer coefficient based on the junction temperature. $R_{spreading}$ represents the additional heat spreading resistance from the cooling interface to the junction surface due to the non-uniform temperature distribution caused by the flow distribution.

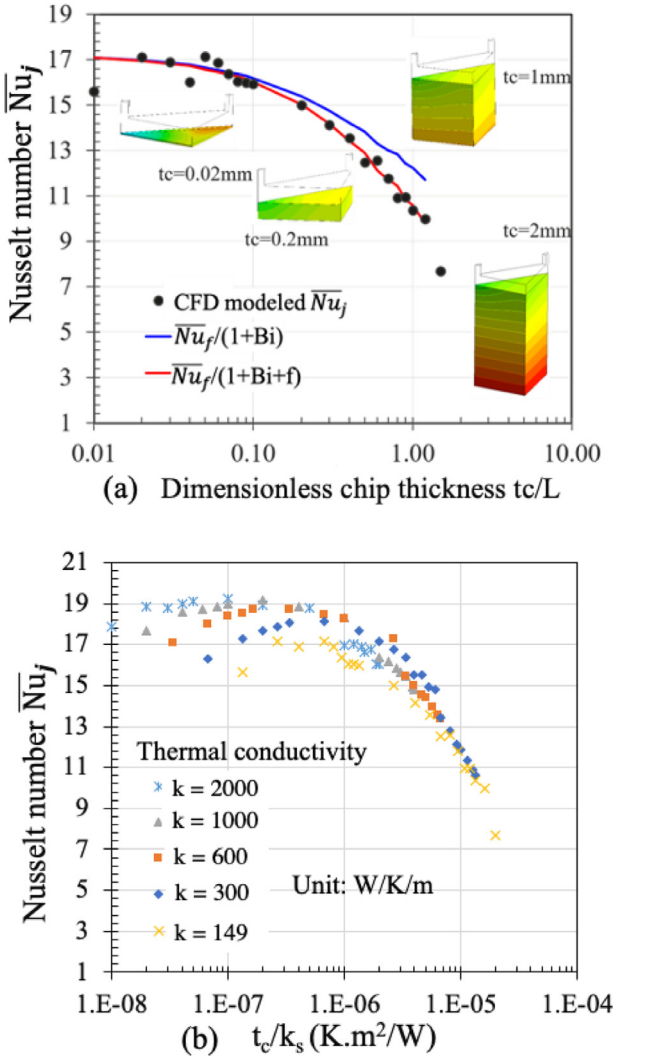

Fig. 4. Effect of the chip thickness on $\overline{Nu}_j$ based on junction temperature for $N = 4$, Re = 1024: (a) $\overline{Nu}_j$ correlation fitting with an additional part $f(t_c, \bar{h}_f, A, k)$ for the silicon substrate with thermal conductivity of 149 W/(m·K); (b) $\overline{Nu}_j$ definition including the substrate conduction for different material thermal conductivity ranging from 149 to 2000 W/(m·K).

Since the Biot number (Bi) is defined as:

$$Bi = \frac{\bar{h}_f}{k_s} * t_c \tag{11}$$

where k_s is the thermal conductivity of the silicon, and k_f is the thermal conductivity of the fluid, Eq. (9) can be rewritten as follows

$$\frac{1}{\bar{h}_j} = \frac{1}{\bar{h}_f} g(Bi) = \frac{1}{\bar{h}_f}\left(1 + Bi + f\left(t_c, \bar{h}_f, A, k\right)\right) \tag{12}$$

In order to get the relation between Nu_j and $f(Bi)$, different values of chip thickness are studied. Fig. 4(a) shows the impact of chip thickness on the heat source junction temperature. With the increase of the chip thickness t_c/L, the $\overline{Nu}_j$ decreases, which shows a clear impact of t_c/L on $\overline{Nu}_j$. Based on the definitions, the $\overline{Nu}_f$ is kept constant for the change of t_c/L, since the heat conduction is decoupled from the equation. As shown in Fig. 4(a), the add term of "$1 + Bi$" could not fully explain the difference between $\overline{Nu}_f$and $\overline{Nu}_j$. Therefore, an additional part $f(t_c, \bar{h}_f, A, k)$ is needed for the heat spreading effects inside the silicon. It can be seen that the "$1 + Bi + f$" can capture the trend very well, shown in Fig. 4(a).

The relation $\overline{Nu}_j$ between $\overline{Nu}_f$ then can be expressed as below:

$$Nu_j = \frac{\overline{Nu}_f}{g(Bi)} = \frac{\overline{Nu}_f}{1 + Bi + \left(0.1Bi + 1.1Bi^2\right)} \tag{13}$$

Most of the effect can be explained by conduction in Si. Additional conduction for extra heat spreading is included in f(Bi). According to the relation $Bi \sim \frac{t_c}{d_i}$, the Bi is more pronounced for very thin Si and for small nozzle diameter, shown in Fig. 4(a).

Practically, for a $\frac{t_c}{L} = 1$, there is about 10% extra reduction between the red curve and blue curve in Fig.4(a), which means that there will be about 35% higher thermal resistance increase for full Si thickness with 2 mm nozzle pitch. Therefore, it can be seen that the heat conduction and spreading resistance in the chip become increasingly dominant for higher values of the chip thickness.

In addition, the Nusselt number $\overline{Nu}_j$ based on the junction temperature including the substrate conduction is investigated for different material thermal conductivity values, ranging from 149 W/(m·K) to 2000 W/(m·K). This range covers most of the substrate materials with different thermal conductivity in electronic applications, including silicon (130-150 W/m/K), SiC (360-490 W/m/K), GaN (130 W/m/K), AlN (285 W/m/K) and diamond (2000 W/m/K) [38]. The Nusselt number $\overline{Nu}_j$ as function of the normalized substrate thickness t_c/k_s is plotted in Fig. 4(b). The simulation results indicate that the $\overline{Nu}_j$ correlation (Eq. (13)) as function of this normalized thickness, which is part of the defined Bi number (eq. 11), still holds for a large range of materials if the t_c/k_s ratio is larger than 1e-6 K.m^2/W, since all the curves with different thermal conductivity collapse in this range.

Therefore, using the expression of Eq. (12), we can use the dimensionless analysis relation $\overline{Nu}_f$-Re_d without considering the impact of the chip thickness, and add the impact of the chip thickness to derive the final value for $\overline{Nu}_j$. on the equation $g(Bi)$. In this way, the design of experiments for the cooler parameter analysis can be simplified for the next sections.

In general, the main objective of the presented study is to provide correlations that can be used as a predictive modeling tool for the thermo-hydraulic performance of the cooler. Since for highly efficient cooling, the relative contribution of the Si substrate becomes significantly more important, we want to include the contribution in the fitted correlation. For the practical application, the chip thickness can vary from full thickness (750 μm) down to several tens of μm. Moreover, experimental results reported in literature are extracted for different Si thicknesses.

The problem with the decoupling of the temperature into a convective and conductive resistance is that the resistance is defined for a uniform temperature, while the flow and temperature distribution of the coolant have an impact on the conduction in the solid Si. The splitting in 3 parts "$1+Bi+(0.1Bi+1.1Bi^2)$ " in Eq. (13) was merely done to demonstrate that the simple conduction resistance is not sufficient to explain the temperature rise and that an extra term is needed to account for the 3D spreading effects.

3.2.2. Effects of nozzle scaling

For the investigation of the nozzle scaling effects, the dimensionless geometry parameters (d_i/L, d_O/L, t/L, H/L) and dimensionless velocity (Re_d) listed in Table 2 are kept the same for different nozzle numbers, ranging from N=1 to N=64. Fig. 5 shows the impact of geometry parameters with different ratios, ranging from 0.01 to 0.4. As shown in Fig. 5(a), the $\overline{Nu}_f$-Re_d curves for all the nozzle numbers collapse for the same dimensionless number. According to the dimensionless theory, the physics should be the same if all the non-dimensional numbers related to geometry parameters and input parameters are kept constant.

As for the $\overline{Nu}_f$-Re_d curves, the relation function can be expressed as following:

$$\overline{Nu}_f = f(x) * Re_d^{0.48*\left(\frac{di}{L}\right)^{-0.16}} \tag{14}$$

where the exponent of Re_d is a function of d_i/L. The correlation $f(x)$ is also a function of the other parameters: d_i/L, d_O/L t/L and H/L, and will be extracted later.

For the $k - Re_d$ correlation curve shown in Fig. 5(b), the impact of the dimensionless variables is also studied when the inlet numbers scale from 1 to 64. It shows that all the $k - Re_d$ curves collapse for α is 0.4, and scatters for smaller values. In addition, it is also observed that the scattering is more pronounced for high Reynolds number.

Fig. 5(c) and 5(d) illustrate one example of the collapse curve when varying the nozzle numbers, for the dimensionless number of 0.1. In order to study the impact of different variables, the inlet number N=4 is chosen for the DOE simulations.

Conclusions can be summarized as below:

- The average Nusselt number $\overline{Nu}_d - Re_d$ curves for different nozzle numbers all collapse for the same dimensionless number ratio. This makes it possible to find a good dimensionless correlation.
- The $k - Re_d$ collapses below $Re_d \leq$1000. At the Reynolds number Re_d higher than 1000, there are discrepancies, especially for smaller α. This means that the pressure drop k-factor correlation cannot be completely captured by the dimensionless analysis.

3.2.3. Effects of nozzle length

In this section, the impact of the nozzle length will be investigated. Literature [36] reported that the flow inside very short nozzle channels (t/L≤ 0.1) would not reach the developed flow regime. Therefore, in the present model, the dimensionless nozzle length is chosen beyond t/L>0.1. Fig. 6 shows the impact of dimensionless nozzle length t/L on the $\overline{Nu}_f$ and f. As illustrated in Fig. 6(a), the $\overline{Nu}_f - \frac{t}{L}$ curve slope is near zero and there is no trend of $\overline{Nu}_f$ with regard to $\frac{t}{L}$. Therefore, the dimensionless nozzle thickness $\frac{t}{L}$ is not included in the final $\overline{Nu}_f$ correlation.

The $k - Re_d$ correlation is shown in Fig. 6(b), which shows that the pressure coefficient factor k increases as the t/L becomes larger. The function between k and t/L for different d_i/L is shown as a linear relationship, as below:

$$k = a * \left(\frac{t}{L}\right) + b \tag{15}$$

In order to understand the effect of nozzle plate thickness, the velocity distribution inside the jet cooling model is studied. It shows that the jet flow distribution at the stagnation and wall jet region does not change as the nozzle length increases, resulting in a stable cooling performance on the heating surface.

3.2.4. Effects of outlet diameter

The impact of the dimensionless outlet diameter is investigated in this section, as shown in Fig. 7. At the same time, the combined effects of d_O/L and H/L of the cavity height are also shown in Fig. 7, indicated as the same color. All the results for different H/L plotted show only small scattering. In this study, the inlet diameter is kept smaller than the outlet diameter to reduce the system pressure drop, which is defined as $d_o/d_i \geq$1. Therefore, a small d_i/L ratio of 0.05 is chosen as the reference value to guarantee that the d_O/L range can cover a larger range for d_o in the analysis. As shown in Fig. 7(a), the Nusselt number keeps stable when the d_O/L is increasing. It can also be seen that the changes of $\overline{Nu}_f$ are very small when the dimensionless cavity height H/L is varied from 0.08

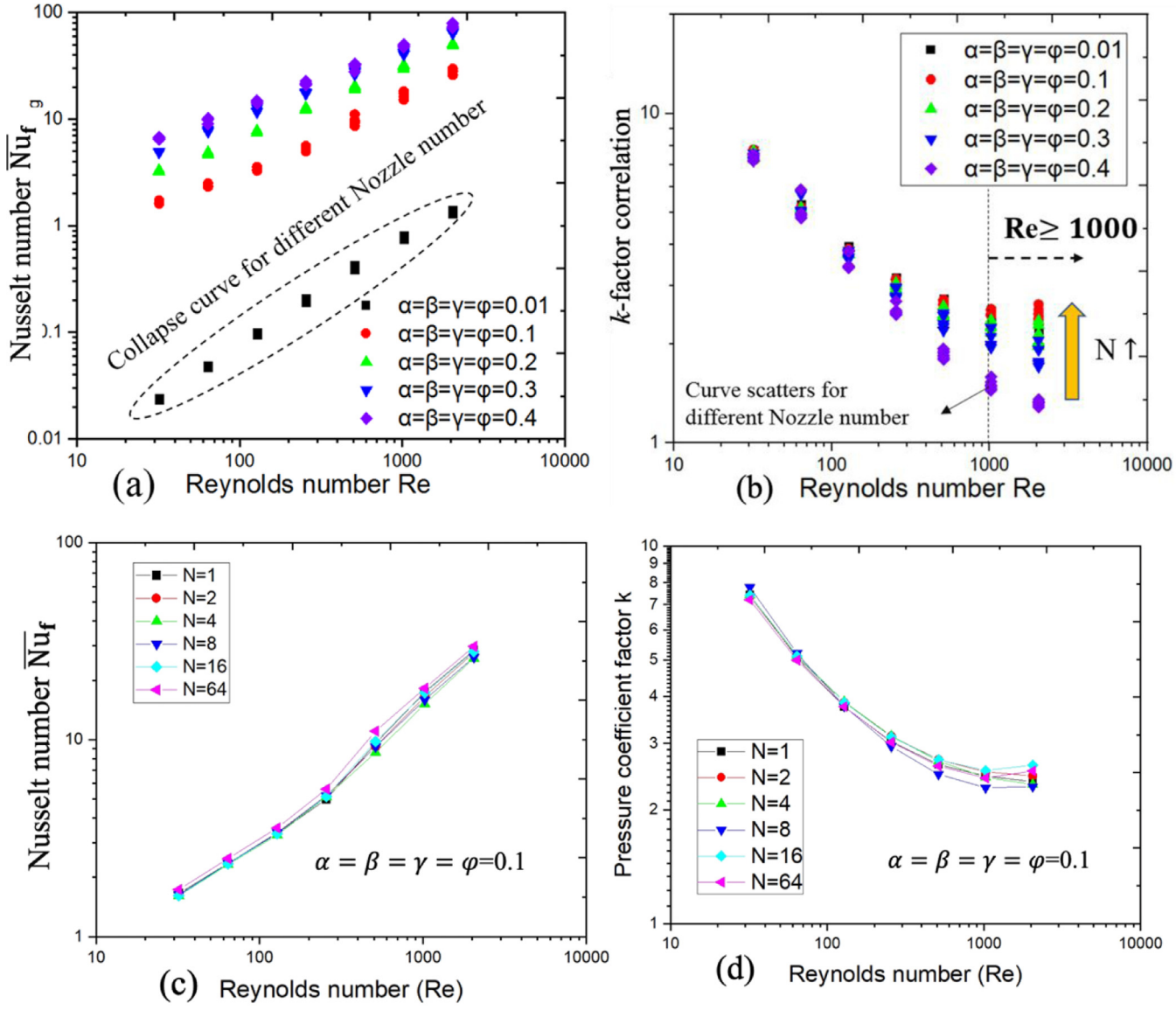

Fig. 5. *N* scaling of the (a) average Nusselt number and (b) pressure drop k-factor as a function of Reynolds number, under different inlet/outlet diameter ratios. (c) and (d) shows the collapse curve includes 6 selected values of *N* (*N* = 1,2,4,8,16,64) for $\alpha = \beta = \gamma = \varphi = 0.1$.

to 0.6. In addition, $\overline{Nu}_f$ becomes larger when the Reynolds number Re_d increases from 32 to 2048, as expected from the $\overline{Nu}_f$-Re_d shown in Fig. 5.

The impact of dimensionless outlet diameter and cavity height on the pressure coefficient factor *k* is shown in Fig. 7(b). It shows that the cavity height has negligible effects on pressure drop, where all the curves with the cavity height varying from 0.08 and 0.6 collapse. Moreveor, the influence of outlet diameter change becomes insignificant beyond d_O/L =0.1. The reason is that the pressure drop inside the outlet nozzles dominates when d_O/L is smaller than 0.1. When d_O/L is higher than 0.1, the pressure drop of the cooler is dominated by the pressure inside the inlet nozzles and impingement cavity. Therefore, there is only impact on the pressure drop for d_O/L smaller than 0.1.

For the Re=512, H/L∈ (0.08, 0.6), d_i/L =0.05, the function of *k* and d_O/L can be expressed as below:

$$k = e^{\left(-28.4*\left(\frac{d_o}{L}\right)\right)} + \varphi(x) \tag{16}$$

where $\varphi(x)$ represents the effects of other parameters.The main conclusions can be summarized as below:

- For $d_o/d_i \geq 1$. the variation of d_o has no impact on $\overline{Nu}_f$-Re_d relation;
  For $d_o/d_i \geq 2$; the d_o has no impact on *k*-Re_d; For $d_o/d_i < 2$, the smaller d_o/L has higher pressure coefficient factor.

The flow behaviors for different outlet diameters are analyzed from the modeling results. In this test case, the ratio d_i/L is chosen as 0.3, where the ratio d_o/L varies from 0.25 to 0.5. The confinement of the flow happens at the nozzle outlet, as the d_o/L =0.25 is smaller than d_i/L =0.3. As the d_o is much smaller than d_i ($d_o \ll d_i$), the pressure drop is higher. However, the pressure drop reduces as the d_o/L becomes larger. On the other hand, the flow regions with stagnation region and wall jet region still keep the same as the d_o/L is increasing. In this study, the impact of the outlet diameter d_o/L is not included in the predictive model within the range of 0.1 to 0.5 since the effects can be negligible under this range.

3.2.5. Effects of cavity height

Fig. 8 shows the jet-to-target ratio H/L effects on heat transfer and pressure drop varying from 0.01 to 2. For the general trend, $\overline{Nu}_f$ and f are both higher for very small cavity heights. For the

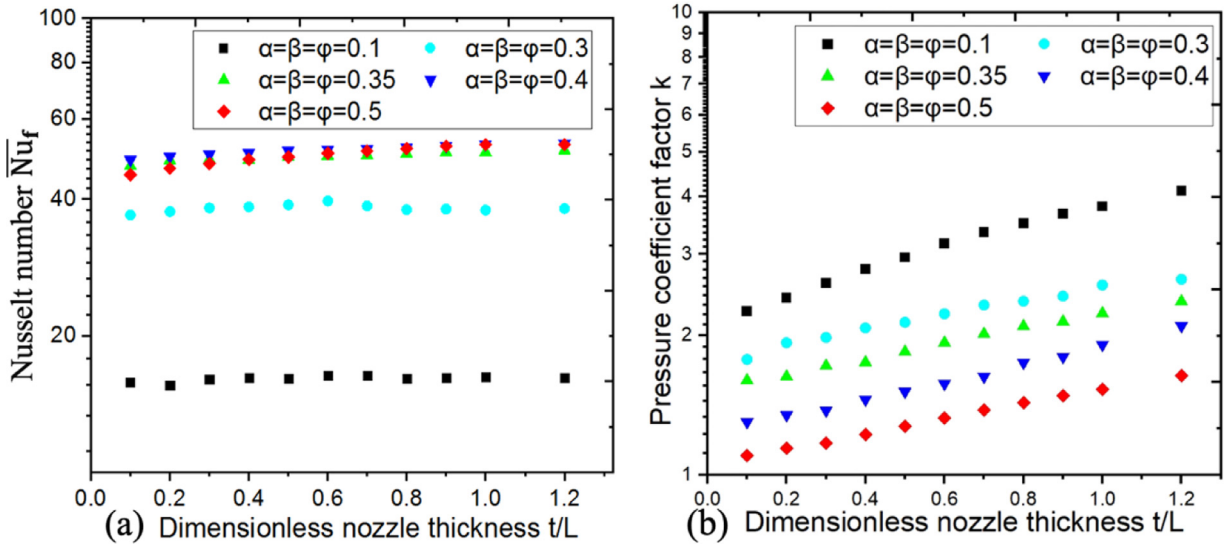

Fig. 6. Impact of dimensionless t/L on the (a) Nusselt number $\overline{Nu}_f$ and (b) Pressure coefficient k under $Re_d = 1024$. Flow distribution for different nozzle length: $Re_d = 1024$, $d_i/L = d_o/L = 0.3$, $H/L = 0.3$.

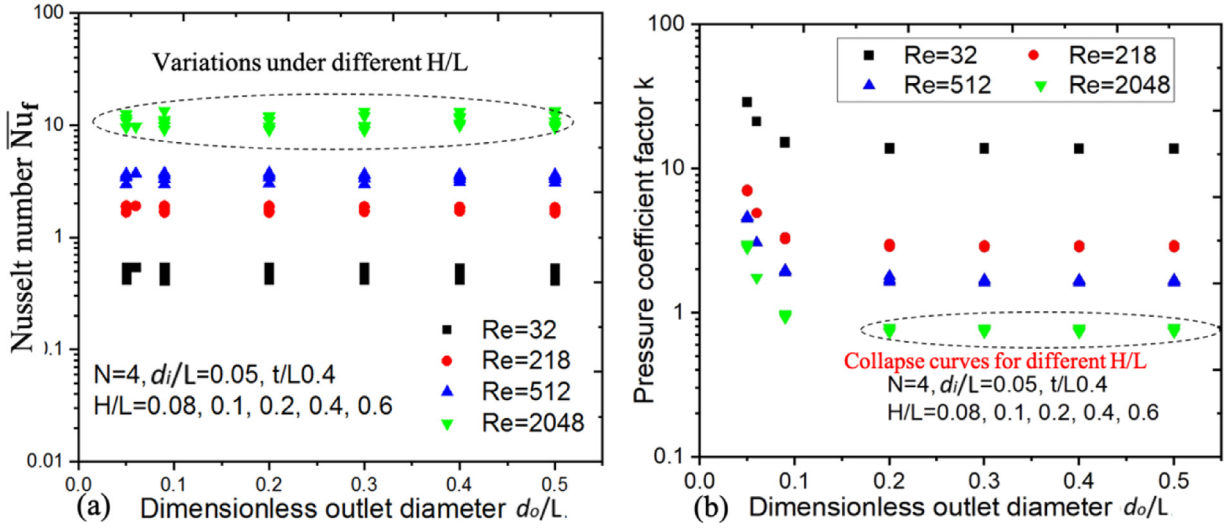

Fig. 7. Impact of outlet diameter ratio on the (a) $\overline{Nu}_f$ and (b) pressure coefficient factor k: $d_i/L = 0.05$; $0.05 \le d_o/L \le 0.5$; $t/L = 0.4$; $d_o/d_i \ge 1$.

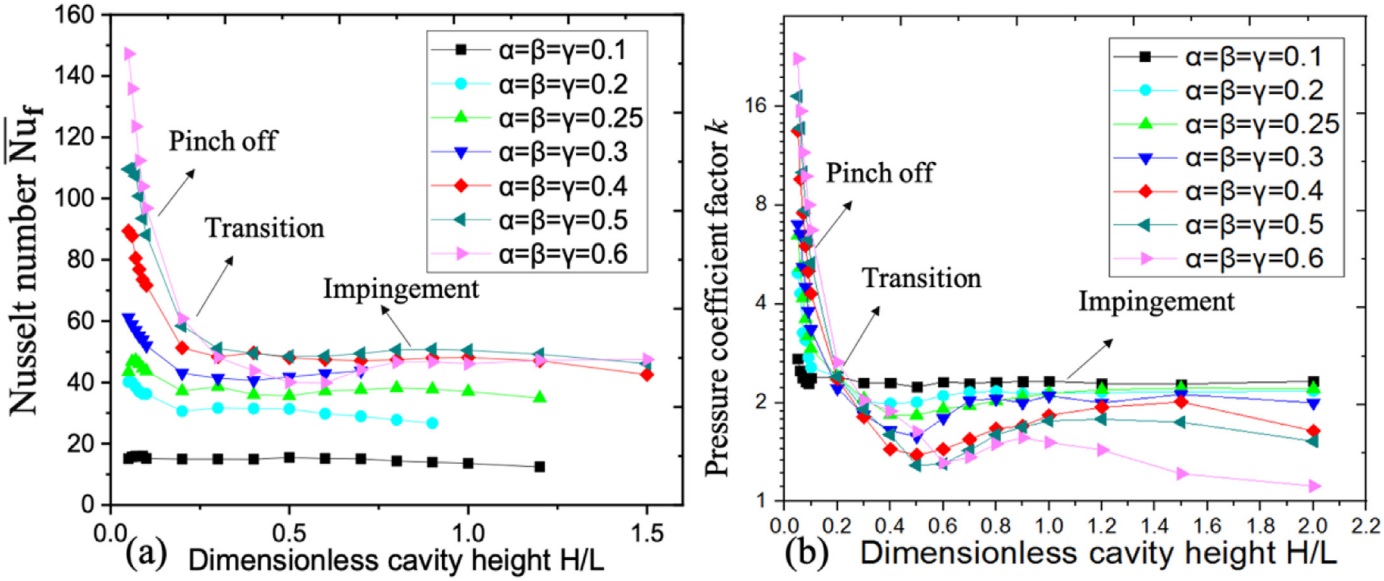

Fig. 8. Effects of cavity height H/L on the (a) $\overline{Nu}_f$ and (b) Pressure coefficient factor k, for a fixed $Re_d = 1024$ ($N = 4$, t/d_i=1, Fl = 600 mL/min, $Re_d = 1024$).

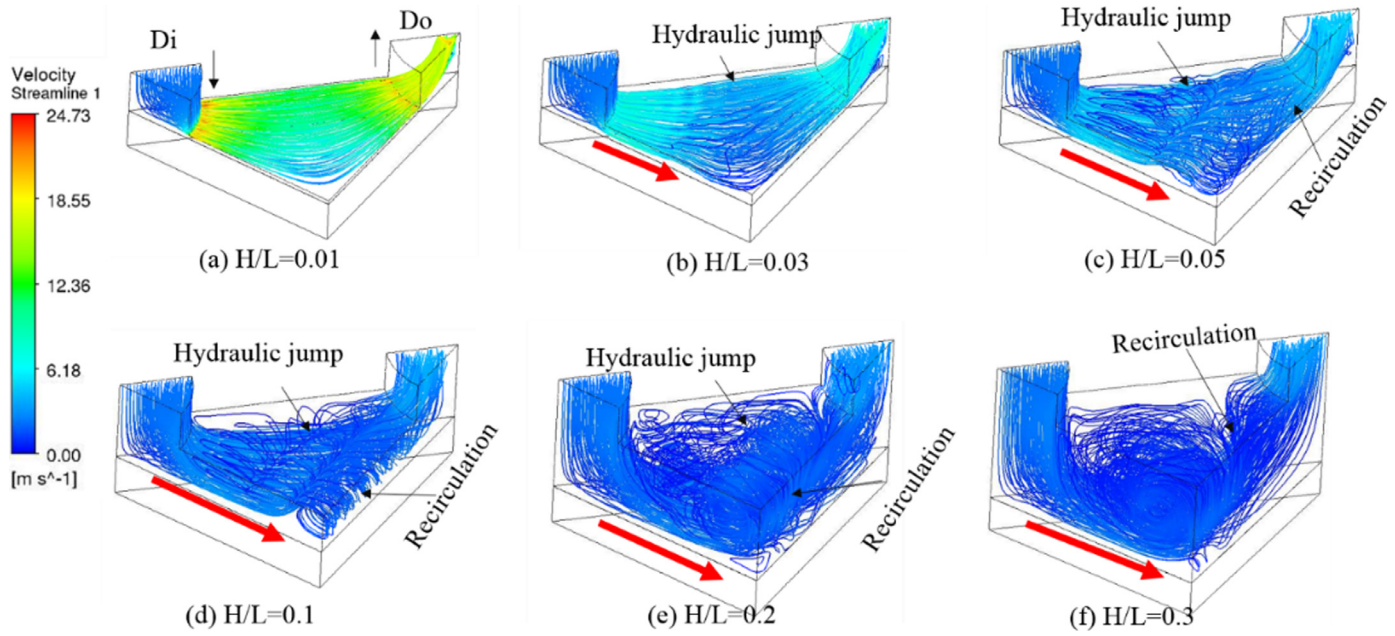

Fig. 9. Impact of the jet-to-target at constant flow ratio: (a) H/L = 0.01; (b) H/L = 0.03; (c) H/L = 0.05; (d) H/L = 0.1; (e) H/L = 0.2; (f) H/L = 0.3. (Reynolds number Re_d = 1024, $d_i/L = d_o/L = 0.3$, t/L = 0.1)

larger cavity height, the $\overline{Nu}_f$ and f keep constant. As for the heat transfer, the Nusselt number $\overline{Nu}_f$ increases with the raise of H/L as the cavity height ratio is below 0.2. This is due to the confining flow as the inlet diameter is much higher than the cavity height channel thickness, resulting in a higher pressure drop and higher flow velocity. There is a minimum value for $\overline{Nu}_f$ and f as the H/L is between 0.1 and 0.5.

For the pressure coefficient factor *k*, there also exists a critical point $H_{critical}/L$ with a minimal *k*. The behavior is more significant for larger inlet diameter ratio d_i/L while the f keeps constant after sharply decreases for smaller d_i/L. For both cases of the heat transfer and pressure drop, it can be seen that the critical point moves toward higher H/L with the increasing of d_i/L. In general, the impact of cavity height on average $\overline{Nu}_f$ and f are very small, for the ratio range: $0.3 \leq H/L < 1$, especially for the small nozzle diameter ratio. For the pressure coefficient factor *k*, the effects of H/L can be neglected when the H/L is higher than $H_{critical}$.

In order to provide insight into how the flow changes for different gap values, CFD simulation results with the unit cell model are shown in Fig. 9. For H/L=0.01, the flow in the cavity height shows like the channel flow dominating most of the jet cooling pressure drop, which is defined as the "Pinch-off" regime in literature [7]. The heat transfer rate is higher inside the cavity height channel, since the boundary layer along the channel is thin. With the increasing of the H, the heat transfer decreases rapidly, as shown in Fig. 8. For H/L=0.03, there is a hydraulic jump around the inlet nozzle region, which is defined as a "transition" regime [7]. The heat transfer will deteriorate due to the thickening of the flow boundary layer [7]. On the other hand, the pressure of the jet cooling decreases due to increasing channel thickness. As H is further increased, the hydraulic jump will move towards the outlet region, as shown in Fig. 9(d). Since the boundary layer is thin before the hydraulic jump and becomes thicker afterward, the heat transfer rate along the chip surface is higher. In addition, there is also "recirculation" around the outlet region. For the cavity height H/L larger than 0.3, the negative effects of hydraulic jump will be reduced, and the heat transfer will keep constant. However, the recirculation flow along the wall jet region becomes more and more dominant, resulting in a higher pressure drop again, as shown in Fig. 9(b). The same physic phenomenon was also observed by Brunschwiler [7]. However, the flow physics used in their study is based on the laminar flow, with Reynolds number ranging from 11 to 402.6. And also, the dimensionless inlet diameter ranges from 0.1 to 0.3. This work extends the laminar flow to transition flow with Re between 32 and 2048. Moreover, this work also covers a wide range of the inlet nozzle diameter ratio d_i/L from 0.1 to 0.6. It is observed that the different flow regimes (pinch-off, transition, impingement) are different for smaller d_i/L and larger d_i/L.

3.2.6. Effects of inlet diameter

As shown in Fig. 10, the impact of inlet nozzle diameter on the $\overline{Nu}_f$ and *k* is investigated, under smaller cavity height ratio H/L=0.5 and higher cavity height H/L=1. In general, the $\overline{Nu}_f$ increases when the inlet diameter ratio d_i/L increases from 0.02 to 0.4. This is attributed to the stagnation region corresponding to the impingement surface becomes larger when the inlet nozzle diameter increases. It is found that the heat transfer coefficient decreases when the jet diameter becomes larger [10]. The impact of inlet diameter was also studied under different Reynolds number varying from 32 to 2048. In the general trend, the $\overline{Nu}_f$-d_i/L presents a good linear function as below:

$$\overline{Nu}_f = \alpha\left(\frac{d_i}{L}\right) + \beta \tag{17}$$

As for the pressure drop coefficient factor, the *k* factor shows power-law function with d_i/L, listed as below:

$$k \sim \left(\frac{d_i}{L}\right)^b \tag{18}$$

3.3. Development of predictive models

As listed in Table 2, the different dimensionless parameters are combined for a full DOE analysis, with more than 1000 simulations for a fixed N with no silicon thickness included. The fittings for $\overline{Nu}_f$-Re_d and *k*-Re_d are derived as function of dimensionless parameters. And the fittings are actually based on the functions found in Section 3.2. As shown in Fig. 5, the pressure drop is extremely high when the normalized inlet diameter ratio comes to 0.01. Therefore,

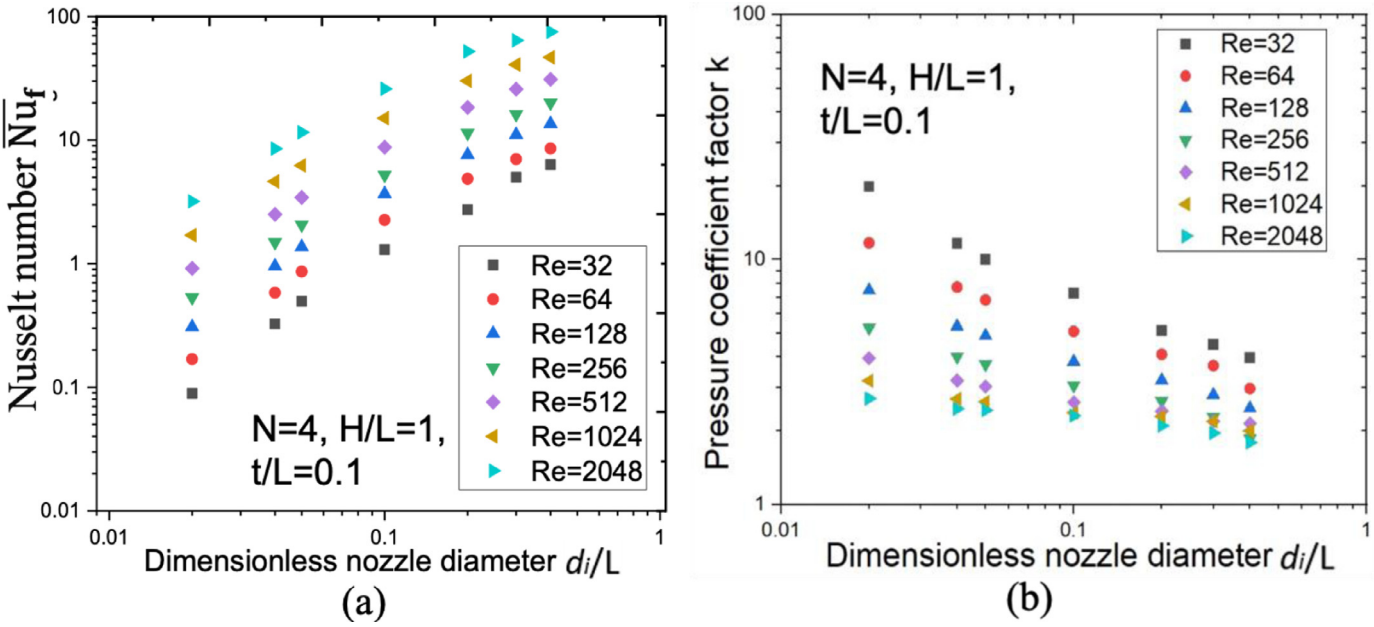

Fig. 10. Nusselt number $\overline{Nu_f}$ (a) and pressure coefficient factor k (b) as a function of dimensionless inlet nozzle diameter, where the t/L = 0.1 and H/L = 1, with larger cavity height ratio (d_i/L = d_O/L).

the dimensional inlet diameter and outlet diameter ratio are chosen above 0.01 in order to keep the pressure drop in the reasonable region.

Based on the multivariable regression analysis, the developed empirical models with $\overline{Nu_f}$-Re_d and k-Re_d are shown below. From the empirical model of $\overline{Nu_f} - Re_d$, the maximum variation is between ±30%. This model also first shows that the exponent of Re_d is as a function of d_i/L. Other parameters such as outlet diameter, cavity height and nozzle plate thickness are negligible when all the parameters are under the confined region.

$$\overline{Nu_f} = \left(5.64\left(\frac{d_i}{L}\right)^2 + 0.031\left(\frac{d_i}{L}\right) - 0.000632\right)\left(\frac{H}{L}\right)^{-0.29} Re_d^{\,0.48\left(\frac{d_i}{L}\right)^{-0.16}} \tag{19}$$

$$\left(\frac{d_i}{L} = \frac{d_o}{L} = a;\ 0.01 \le a \le 0.4;\ 0.01 \le H/L \le 0.4;\ 32 \le Re_d \le 2048;\ 0.05 \le H/d_i \le 20;\ 0.01 \le t/L \le 0.4\right)$$

The pressure coefficient factor k correlations with the predictive error between ±30% is also developed as below:

$$k = \left\{\left(21.2*\left(\frac{d_i}{L}\right) + 14.5\right)Re_d^{\,-0.73\left(\frac{d_i}{L}\right)-0.26}\left(2.26\left(\frac{t}{L}\right) + 0.89\right)\left(0.37\left(\frac{H}{L}\right)0.15 + 0.55\right) + 0.8\right\} \tag{20}$$

$$\left(\frac{d_i}{L} = \frac{d_o}{L} = a;\ 0.05 \le a \le 0.6;\ 0.5 \le H/d_i \le 20;\ 32 \le Re_d \le 1024;\ t/L \ge 0.1\right)$$

For the k -Re empirical model, it can be seen that k has a linear relationship with the t/L. The effects of the cavity are also captured by the developed function. In Fig. 11, the evaluation of the fitting agreement for all simulation results of the DOE is presented.

4. Experimental validations of predictive model

In order to validate the Nu correlations with Eq. (19) derived in this paper, 2 different impingement coolers with large different in nozzle dimensions are validated with the experimental data. The first one is our own demonstrator of 3D printed polymer cooler with 300-750 μm nozzles [35] for three different nozzle arrays.

As shown in the previous study [35], a simplified board level polymer demonstrator cooler with a 4 × 4 array of 750 μm inlets and 5 × 5 array of 750 μm outlets has been demonstrated and measured. The 3D printed chip cooler has been successfully mounted to the chip package and no leakage is observed, illustrated in Fig. 12. Temperature measurements are performed using the 32 × 32 array of diodes in the in-house Packaging Test Chip Version Q (PTCQ) thermal test chip to visualize the chip temperature distribution for the quasi-uniform power dissipation pattern. The 95% confidence interval of the calibrated sensitivity of the temperature sensor on the test chip is - 1.55 ± 0.02 mV/°C in the temperature range between 10 and 75 °C for a current of 5 μA. A dedicated closed flow loop is built to characterize the thermal and hydraulic performance of the cooler. The fluid used in this measurement is Deionized water (DI water). The flow rate in the system is controlled by a mini-Cori flow meter with accuracy of ± 0.2% as a percentage of reading (%RD). The pressure drop between the inlet and outlet is measured by a differential pressure gauge that can withstand a static pressure of 10 bar. The scope of the pressure drop is between 0.2 and 5 bar with an accuracy < ±0.5% as a percentage of full scale (% FS). A stainless-steel basket filter is used for the pump with a screen of 25 μm. The analysis of the propagated measurement uncertainty results in a value of ± 1.8 % for the reported thermal measurements [35]. The measured cooling performance of the 3D printed coolers with 3 × 3, 4 × 4, and 8 × 8 inlet nozzle arrays are characterized in this paper. The second one is the Si impingement cooler with 43 µm diameter nozzles. The measurement data are extracted from the literature [7].

The demonstrations of the three coolers [38] and also the silicon impingement jet cooler [7] are all shown in Fig. 13. Table 3 lists the comparison between the designed value and measured value of the nozzle diameters for the three coolers. Also, the di-

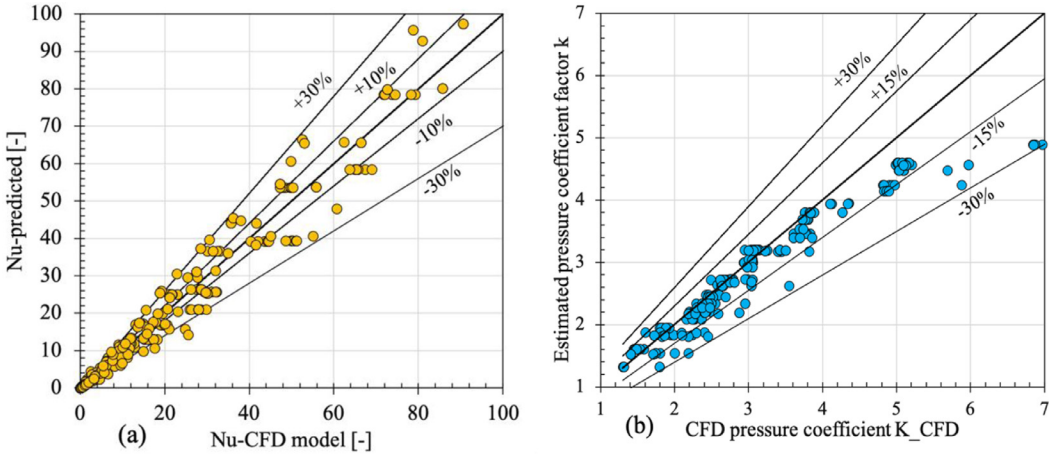

Fig. 11. Correlations fitting for heat transfer and flow dynamics: (a) developed $\overline{Nu}_f$ correlation versus CFD $\overline{Nu}_f$ data (b) developed k factor correlation versus k_CFD.

Table 3
Comparison between the designed and fabricated parameters (unit: mm).

N × N array	Unit cell	d_i (Design)	d_i (Meas.)	d_i/L (Meas.)	H/L(Meas.)
3 × 3	2.67 mm	0.8 mm	0.95 mm	0.36	0.33
4 × 4	2 mm	0.6 mm	0.75 mm	0.375	0.33
8 × 8	1mm	0.3 mm	0.38 mm	0.38	0.33
19044 [7]	0.15 mm		0.043 mm	0.287	0.33

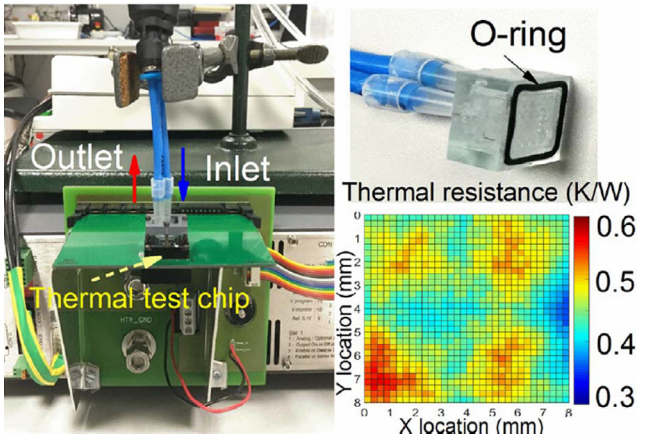

Fig. 12. Experimental setup and cooler assembly with the thermal test vehicles.

mensionless number di/L with the measured values are also listed. Since the cavity height designed for all the three coolers are measured as the same value with 650 μm, the dimensionless number H/L used in the predictive model is H/L=0.33. In general, it can be seen that the measured di/L is a bit lager than the designed value of d_i/L =0.3. For the predictive model validation, the measured thermal resistance and flow rate are all transformed to the $\overline{Nu}_f$-Re_dcorrelations. The plotted $\overline{Nu}_f$-Re_d relations for the coolers with three different inlet nozzle arrays are used to validate the predictive model, based on the dimensionless analysis. As shown in Fig. 14, it can be seen that the predictive model based on the measured di/L value listed in Table 3 shows a good agreement with the experimental results.

Moreover, the measurement data from Brunschwiler et al. are also used to validate our developed predictive model, as shown in Fig. 15. The cooler parameters from Brunschwiler et al. [7] are imported into the predictive model, where the nozzle diameter is 43

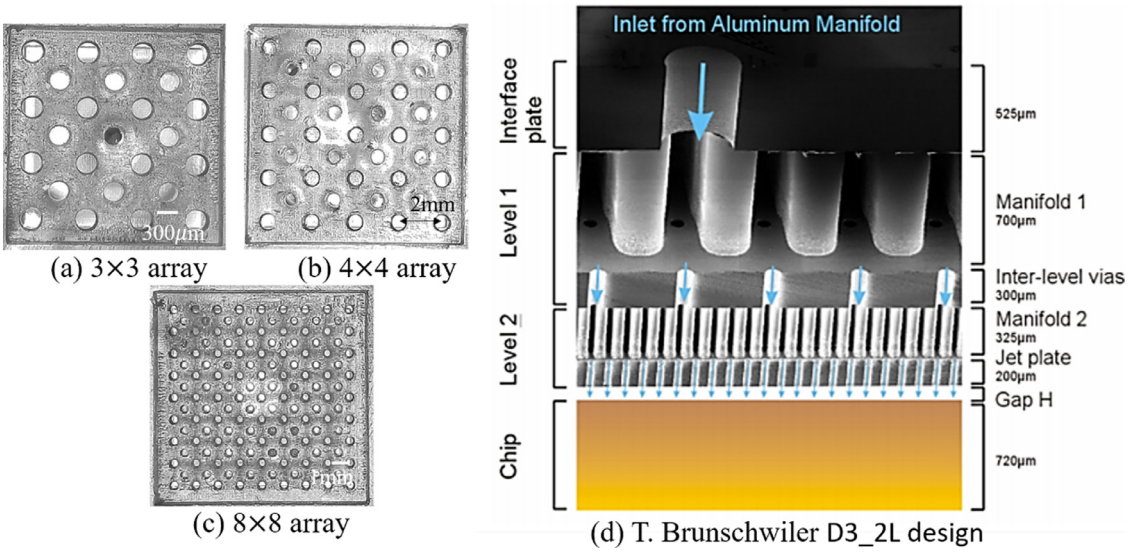

Fig. 13. Demonstrations of the three different version 3D printed coolers with (a) 3 × 3; (b) 4 × 4 and (c) 8 × 8; and also (d) the silicon based jet cooler with 19,044 nozzles from Brunschwiler et al. [7].

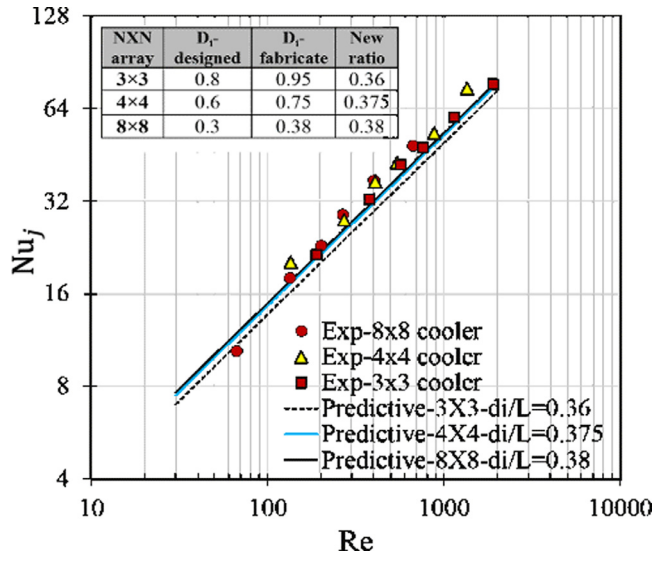

Fig. 14. Comparison of the measurements data and developed predictive model $\overline{Nu}_j$-Re_d for the 3D printed coolers with 3 × 3, 4 × 4 and 8 × 8 inlet nozzle arrays.

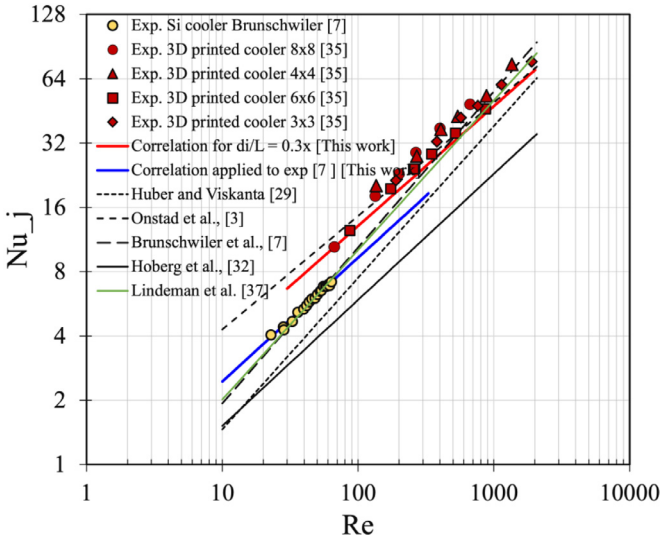

Fig. 15. Comparison of the developed predictive model with literature experimental data and correlations.

μm, unit cell length is 150 μm, and the nozzle number is 19044. It can be seen that the predicted $\overline{Nu}_f$-Re_d curve based on the geometry parameters shows good agreement with the experimental data in the literature [7], and this agreement is better than their $\overline{Nu}_f$-Re_d correlation. This is because the impacts of the d_i/L and H/L are included in our predictive model. Furthermore, the extracted $\overline{Nu}_f$-Re_d correlation is also compared with the state of art $\overline{Nu}_f$-Re_d correlations in the literature based on the 3D printed cooler configurations, as reviewed in Section 1.2. It can be seen that the most matched developed model is Onstad's model [3], while the difference is larger for other models. However, the empirical constants for the power-law relationship of Nu_D versus Re_D for Onstad's model are only limited to three different nozzle diameter values. Moreover, it is also found that the predictive model developed by Lindeman et al. [37] shows nicely predication in the large Reynolds region above 1000, but larger error in the small Reynolds number region. It should be noted that our developed model is based on the jet cooling with locally distributed outlets, which includes the dimensionless term of d_i/L and H/L. The developed Nu-Re model applies to different d_i/L and H/L ratios, under the range ($0.01 \leq d_i/L \leq 0.4$; $0.01 \leq H/L \leq 0.4$). In summary, the predictive model including the effects of d_i/L and H/L matches well with our in-house developed experimental results and also shows good agreement with the available experimental Brunschwiler et al. data.

5. Conclusions

In this paper, non-dimensional correlations are developed for the heat transfer in terms of the Nusselt number $\overline{Nu}_f$ and pressure coefficient factor k as a function of the dimensionless geometrical parameters for direct on-chip microscale liquid jet impingement cooling with alternating feeding and draining nozzles. Those correlations can be used as a predictive model to estimate the thermal and hydraulic performance of a jet impingement cooler with an N × N array on inlet nozzles and a N+1 × N+1 array of outlet nozzles distributed between the inlet nozzles. The dimensionless analysis is performed using conjugated heat transfer and fluid flow unit cell CFD models using a transition SST turbulence model, which has been validated with LES simulations [34]. An extensive design of experiments analysis (DOE) has been performed based on the listed dimensionless geometry parameters (d_i/L, d_O/L, t/L, H/L) and dimensionless velocity (Re_d) to create the data set for the fitting of the correlations.

In the first step, the impact of the individual geometrical parameters has been studied and a fitting function has been proposed to describe this impact. This study showed that the impact of the chip thickness has a significant impact on the junction temperature of the application and that the relative impact of this contribution increases as the convective heat transfer increases. Due to the non-uniformity and the jet impingement flow and the chip surface temperature distribution, this impact is larger than just the contribution of the one-dimensional conduction through the silicon of the chip, but also includes significant contributions of additional lateral heat spreading. Moreover, the effects of the nozzle length, outlet diameter and cavity height are studied and quantified in this work.

In the second step, the Nusselt number and k-factor correlations are fitted for all the dimensionless parameters based on the previously derived functions for the individual parameters. The fitted correlations show maximum predictive error of ±30% for the $\overline{Nu}_f$ and the pressure coefficient k factor correlation respectively, based on a comparison of the fitted values with the simulation values. The Nusselt number $\overline{Nu}_f$ correlation has been experimentally validated for both own test vehicle data of jet impingement coolers with distribution nozzles with a nozzle diameter range of 300 – 800 µm, as well as for literature data for smaller 43 µm diameter nozzles. For both sets of experiments, the developed correlations show a very good agreement with the experimental data over the Re range from 20 to 2000.

Declaration of Competing Interest

The authors declare that they have no known competing financial interests or personal relationships that could have appeared to influence the work reported in this paper.

CRediT authorship contribution statement

Tiwei Wei: Writing – review & editing, Investigation, Data curation, Methodology. **Herman Oprins:** Supervision, Resources, Writing – review & editing. **Liang Fang:** Software. **Vladimir Cherman:** Methodology. **Eric Beyne:** Conceptualization, Funding acquisition. **M. Baelmans:** Conceptualization, Supervision.

References

[1] Tiwei W., 2020. "ll-in-one design integrates microfluidic cooling into electronic chips," Nature, vol. 585(7824), pages 188-189, September.
[2] J.F. Maddox, R.W. Knight, S.H. Bhavnani, Local thermal measurements of a confined array of impinging liquid jets for power electronics cooling, in: Proceedings of the 31st Thermal Measurement, Modeling & Management Symposium (SEMI-THERM), 2015, pp. 228–234.
[3] AJ. Onstad, et al., Flow and Heat Transfer for Jet Impingement Arrays with Local Extraction, in: Proceedings of the Sixth International Symposium on Turbulence and Shear Flow Phenomena, Begel House Inc., 2009, pp. 315–320.
[4] D.M. Kercher, W. Tabakoff, Heat transfer by a square array of round air jets impinging perpendicular to a flat surface including the effect of spent air, J. Eng. Power. Jan 92 (1) (1970) 73–82.
[5] L.W. Florschuetz, DE. Metzger, Jet array impingement with crossflow-correlation of streamwise resolved flow and heat transfer distributions, Final Report, Arizona State Univ, Tempe, 1981.
[6] B.R. Hollworth, Arrays of impinging jets with spent fluid removal through vent holes on the target surface—Part 1: Average heat transfer, (1980): J. Eng. Power. 102 (4) (Oct 1980) 994–999.
[7] T. Brunschwiler, et al., Direct liquid jet-impingement cooling with micronsized nozzle array and distributed return architecture, in: Proceedings of the IEEE InterSociety Conference on Thermal and Thermomechanical Phenomena in Electronic Systems, 2006, pp. 196–203.
[8] T. Tiwei, et al., High efficiency direct liquid jet impingement cooling of high power devices using a 3D-shaped polymer cooler, in: Proceedings of the IEEE International Electron Devices Meeting (IEDM), IEEE, 2017.
[9] A.K. Shukla, A. Dewan, Flow and thermal characteristics of jet impingement: comprehensive review, Int. J. Heat Technol. 35 (1) (2017) 153–166.
[10] B.L. Button, K. Jambunathan, in: Jet Impingement Heat Transfer: A Bibliography 1976–1985, 15, Previews Heat Mass Transfer, 1989, pp. 149–178.
[11] K. Jambunathan, et al., A review of heat transfer data for single circular jet impingement, Int. J. Heat Fluid Flow 13.2 (1992) 106–115.
[12] N. Zuckerman, N. Lior, Jet impingement heat transfer: physics, correlations, and numerical modeling, Adv. Heat Trans. 39 (2006) 565–631.
[13] S.V. Garimella, R.A. Rice, Confined and submerged liquid jet impingement heat transfer, J. Heat Transf. 117 (4) (1995) 871–877, doi:10.1115/1.2836304.
[14] D.J. Womac, S. Ramadhyani, F.P. Incropera, Correlating equations for impingement cooling of small heat sources with single circular liquid jets, J. Heat Transf. 115 (1) (1993) 106–115.
[15] H. Martin, Impinging jets, in: Heat Exchanger Design Handbook, 2, Hemisphere Publishing Corporation., 1983, pp. 2–5.
[16] W. Tiwei, et al., Experimental characterization and model validation of liquid jet impingement cooling using a high spatial resolution and programmable thermal test chip, Appl. Thermal Eng. 152 (2019) 308–318.
[17] B. Weigand, S. Spring, Multiple jet impingement– a review. In TURBINE-09, in: Proceedings of the International Symposium on Heat Transfer in Gas Turbine Systems, 2009, pp. 101–142.
[18] S.V. Narumanchi, V. Hassani, D. Bharathan, Modeling Single-Phase and Boiling Liquid Jet Impingement Cooling in Power Electronics (No. NREL/TP-540-38787), National Renewable Energy Lab.(NREL), Golden, CO (United States), 2005.
[19] B.P. Whelan, A.J. Robinson, Nozzle geometry effects in liquid jet array impingement, Appl. Thermal Eng. 29 (11-12) (2009) 2211–2221.
[20] A. Royne, C.J. Dey, Effect of nozzle geometry on pressure drop and heat transfer in submerged jet arrays, Int. J. Heat Mass Transf. 49 (3-4) (2006) 800–804.
[21] K. Azar, et al., Electronics Cooling and the Need for Experimentation, in: Thermal Measurements in Electronics Cooling, 1st, CRC Press, Boca Raton, 1997, pp. 10–43.
[22] M. Molana, S. Banooni, Investigation of heat transfer processes involved liquid impingement jets: a review, Brazil. J. Chem. Eng. 30 (3) (2013) 413–435.
[23] H. Martin, Heat and mass transfer between impinging gas jets and solid surfaces, Adv. Heat Transf. 13 (1977) 1–60.
[24] V.A. Patil, V. Narayanan, Spatially resolved heat transfer rates in an impinging circular microscale jet, Microscale Thermophys. Eng. 9 (2) (2005) 183–197.
[25] D.J. Womac, F.P. Incropera, SS. Ramadhyani, Correlating equations for impingement cooling of small heat sources with multiple circular liquid jets, ASME. J. Heat Transfer. 116 (2) (1994) 482–486, doi:10.1115/1.2911423.
[26] A.J. Robinson, E. Schnitzler, An experimental investigation of free and submerged miniature liquid jet array impingement heat transfer, Experimen. Thermal Fluid Sci. 32 (1) (2007) 1–13.
[27] Y. Pan, B.W. Webb, Heat transfer characteristics of arrays of free-surface liquid jets, (1995): J. Heat Transfer. 117 (4) (Nov 1995) 878–883.
[28] M. Fabbri, V.K. Dhir, Optimized heat transfer for high power electronic cooling using arrays of microjets, J. Heat Transf. 127 (2005) (2005) 760–769.
[29] A.A.M. Huber, R. Viskanta, Effect of jet–jet spacing on convective heat transfer to confined, impinging arrays of axisymmetric air jets, Int. J. Heat Mass Transf. 37 (18) (1994) 2859–2869.
[30] D. Rhee, P. Yoon, H. Cho, Local heat/mass transfer and flow characteristics of array impinging jets with effusion holes ejecting spent air, Int. J. Heat Mass Transf. 46 (6) (2003) 1049–1061.
[31] A. Onstad, C. Elkins, R. Moffat, Full-field flow measurements and heat transfer of a compact jet impingement array with local extraction of spent fluid, ASME J. Heat Transf. 131 (8) (2009) 082201.
[32] T.B. Hoberg, A.J. Onstad, J.K. Eaton, Heat transfer measurements for jet impingement arrays with local extraction, Int. J. Heat Fluid Flow 31 (3) (2010) 460–467.
[33] A.S. Rattner, General characterization of jet impingement array heat sinks with interspersed fluid extraction ports for uniform high-flux cooling, J. Heat Transf. 139 (8) (2017) pp. 082201/1–082201/11.
[34] W. Tiwei, et al., in: "Conjugate Heat Transfer and Fluid Flow Modeling for Liquid Microjet Impingement Cooling with Alternating Feeding and Draining Channels", 4, Fluids, 2019, p. 145.
[35] W. Tiwei, et al., Nozzle scaling effects for the thermohydraulic performance of microjet impingement cooling with distributed returns, Appl. Thermal Eng. 180 (2020) 115767.
[36] B. Kashi, D.H. Haustein, Dependence of submerged jet heat transfer on nozzle length, Int. J. Heat Mass Transf. 121 (2018) 137–152.
[37] B.A. Lindeman, J.M. Anderson, T.A. Shedd, Predictive model for heat transfer performance of oblique and normally impinging jet arrays, Int. J. Heat Mass Transf. 62 (2013) 612–619.
[38] V. Cimalla, J. Pezoldt, O. Ambacher, Group III nitride and SiC based MEMS and NEMS: materials properties, technology and applications, J. Phys. D Appl. Phys. 40 (20) (2007) 6386.
[39] B. Elison, B.W. Webb, Local heat transfer to impinging liquid jets in the initially laminar, transitional, and turbulent regimes – ScienceDirect, Int J Heat Mass Transf 37 (1994) 1207–1216.
[40] C.-Y. Li, S.V. Garimella, Prandtl-Number Effects and Generalized Correlations for Confined and Submerged Jet Impingement, International Journal of Heat and Mass Transfer 44 (18) (2001) 3471–3480.
[41] A.J. Robinson, E. Schnitzler, An experimental investigation of free and submerged miniature liquid jet array impingement heat transfer, Experimental Thermal and Fluid Science 32 (1) (2007) 1–13.
[42] C. Meola, A new correlation of Nusselt number for impinging jets, Heat Transfer Engineering 30 (3) (2009) 221–228.
[43] P. Tie, Q. Li, Y. Xuan, Investigation on the submerged liquid jet arrays impingement cooling, Applied thermal engineering 31 (14-15) (2011) 2757–2763.
[44] N. Yonehara, I. Ito, Cooling characteristics of impinging multiple water jets on a horizontal plane, Technol. Rep. Kansai University 24 (1982) 267–281.
[45] L.J. Jiji, Z. Dagan, Experimental Investigation of Single-Phase Multijet Impingement Cooling of an Array of Microelectronic Heat Sources, in: Proceedings of the International Symposium on Cooling Technology for Electronic Equipment, W. Aung, Washington, D.C., Hemisphere Publishing Corporation, 1987, pp. 333–351.
[46] D.T. Vader, F.P. Incropera, R. Viskanta, Local convective heat transfer from a heated surface to an impinging planar jet of water, Int. J. Heat Mass Transfer 34 (1991) 611–623.
[47] X. Liu, V.J.H. Lienhard, J.S. Lombara, Convective heat transfer by impingement of circular liquid jets, J. Heat Transfer 113 (1991) 571–582.
[48] G.J. Michna, et al., The. Effect of Area Ration on Microjet Array Heat Transfer, International Journal of Heat and Mass Transfer 54 (2011) 1782–1790.
[49] T. Muszynski, R. Andrzejczyk, Heat transfer characteristics of hybrid microjet–microchannel cooling module, Applied Thermal Engineering 93 (2016) 1360–1366.